Supplementary Information

Unravelling the mechanism of polarization transfer from spin-1/2 to spin-1 system in solids

Ekta Nehra[1] and Manoj Kumar Pandey*[1]

[1]Department of Chemistry, Indian Institute of Technology Ropar, Rupnagar, Punjab, 140001, India.
(* *Electronic mail: mkpandey@iitrpr.ac.in*)

Part-1

I Description of CP spin dynamics based on existing reports

From equation (10) (in the main text), the CP Hamiltonian during the mixing (spin-locking/contact) period under the on-resonance S-spin irradiation is given as

$$\begin{aligned}\hat{\tilde{\tilde{\tilde{H}}}} = \Big(\frac{\omega_e-\omega_Q}{4}\Big)\big[\hat{S}_z^{13}+\hat{S}_z^{46}\big]+\Big(\frac{3\omega_e+\omega_Q}{12}\Big)\big[\hat{S}_z^{12}-\hat{S}_z^{23}+\hat{S}_z^{45}-\hat{S}_z^{56}\big]+\omega_{1I}\big[\hat{S}_z^{14}+\hat{S}_z^{25}+\hat{S}_z^{36}\big]\\ +2\omega_d\cos\theta_1/2\big[\hat{S}_x^{16}+\hat{S}_x^{34}\big]-2\omega_d\sin\theta_1/2\big[\hat{S}_x^{26}+\hat{S}_x^{35}\big].\end{aligned} \tag{A1}$$

To explain the experimental results obtained from CP experiments, Pratum and Klein proposed an approach, wherein, the above Hamiltonian was re-expressed in two forms. In the first approach, the Hamiltonian was expressed in the TQ-SQ subspace ignoring the dipolar contributions resulting from the ZQ-DQ operators. Employing such an approach, the CP dynamics corresponding to the SQ matching condition was described qualitatively without any analytic expression. In the second approach, the same Hamiltonian was re-expressed in the ZQ-DQ subspace ignoring the dipolar contributions emerging from the TQ-SQ operators. While such an approach, presents a qualitative description of the CP dynamics observed in experiments, the method is of limited utility in quantifying the experimental data. Below, we present a brief description of the signal expressions derived from the effective Hamiltonians using their approach.

Method I: Description of the CP dynamics in the triple and single-quantum (TQ+SQ) sub-spaces

To describe the spin dynamics corresponding to the SQ and TQ matching conditions, the Hamiltonian in Eq. (A1) is re-expressed in terms of the TQ/SQ operators.

$$\hat{\tilde{\tilde{\tilde{H}}}}_{16,34} \approx \Sigma\big[\hat{S}_z^{16}\big]+\omega_{IS}\big[\hat{S}_x^{16}\big]+\Delta\big[\hat{S}_z^{34}\big]+\omega_{IS}\big[\hat{S}_x^{34}\big]+\omega_{1I}\big[\hat{S}_z^{25}\big]+\Big(\frac{3\omega_e+\omega_Q}{12}\Big)\big[\hat{S}_z^{12}-\hat{S}_z^{23}+\hat{S}_z^{45}-\hat{S}_z^{56}\big] \tag{A2}$$

where $\Sigma=\Big\{\dfrac{4\omega_{1I}+(\omega_e-\omega_Q)}{4}\Big\}$, $\Delta=\Big\{\dfrac{4\omega_{1I}-(\omega_e-\omega_Q)}{4}\Big\}$, and $\omega_{IS}=2\omega_d\cos\theta_1/2$.
Employing the effective field approach described in the main section, the above Hamiltonian is diagonalized sequentially and the final form of the signal observed in CP experiments is derived and summarized below:

$$\hat{H}_{e,16,34}=\omega_{e,16}\big[\hat{S}_z^{16}\big]+\omega_{e,34}\big[\hat{S}_z^{34}\big]+\omega_{1I}\big[\hat{S}_z^{25}\big]+\Big(\frac{3\omega_e+\omega_Q}{12}\Big)\big[\hat{S}_z^{12}-\hat{S}_z^{23}+\hat{S}_z^{45}-\hat{S}_z^{56}\big] \tag{A3}$$

where $\omega_{e,16}=\sqrt{\Sigma^2+\omega_{IS}^2}$ and $\omega_{e,34}=\sqrt{\Delta^2+\omega_{IS}^2}$.
Using the density operator formalism, the signal expression in the TQ+SQ space is given as

$$S(t)_{16,34}=\langle\hat{S}_{e,x}(t)\rangle=\frac{4\omega_{1S}}{\omega_e}\Bigg[\underbrace{-\frac{\omega_{IS}^2}{\Sigma^2+\omega_{IS}^2}\sin^2\frac{\sqrt{\Sigma^2+\omega_{IS}^2}}{2}t}_{TQ}+\underbrace{\frac{\omega_{IS}^2}{\Delta^2+\omega_{IS}^2}\sin^2\frac{\sqrt{\Delta^2+\omega_{IS}^2}}{2}t}_{SQ}\Bigg]. \tag{A4}$$

Method II: Description of the CP dynamics in the zero and double-quantum (ZQ+DQ) sub-spaces

In a similar vein, to describe the CP dynamics in the ZQ-DQ subspace, Eq. (A1) is re-expressed in terms of the ZQ/DQ operators.

$$\tilde{\tilde{\hat{H}}}_{35,26} \approx \Sigma' \left[\hat{S}_z^{35}\right] + \omega'_{IS}\left[\hat{S}_x^{35}\right] + \Delta'\left[\hat{S}_z^{26}\right] + \omega'_{IS}\left[\hat{S}_x^{26}\right] + \omega_{1I}\left[\hat{S}_z^{14}\right] + \left(\frac{3\omega_e - \omega_Q}{12}\right)\left[\hat{S}_z^{12} + \hat{S}_z^{13} + \hat{S}_z^{45} + \hat{S}_z^{46}\right] \tag{A5}$$

where $\Sigma' = \left\{\frac{4\omega_{1I} + (\omega_e + \omega_Q)}{4}\right\}$, $\Delta' = \left\{\frac{4\omega_{1I} - (\omega_e + \omega_Q)}{4}\right\}$, and $\omega'_{IS} = -2\omega_d \sin\theta_1/2$.

Employing the effective field approach, the above Hamiltonian is diagonalized and the final form of the signal observed in CP experiments is derived and summarized below:

$$\hat{H}_{e,35,26} = \omega_{e,35}\left[\hat{S}_z^{35}\right] + \omega_{e,26}\left[\hat{S}_z^{26}\right] + \omega_{1I}\left[\hat{S}_z^{14}\right] + \left(\frac{3\omega_e - \omega_Q}{12}\right)\left[\hat{S}_z^{12} + \hat{S}_z^{13} + \hat{S}_z^{45} + \hat{S}_z^{46}\right] \tag{A6}$$

where $\omega_{e,35} = \sqrt{\Sigma'^2 + \omega'^2_{IS}}$ and $\omega_{e,26} = \sqrt{\Delta'^2 + \omega'^2_{IS}}$.
Utilizing the density operator formalism, the signal expression in the ZQ+DQ space is given as

$$S(t)_{35,26} = \frac{4\omega_{1S}}{\omega_e}\left[\underbrace{-\frac{\omega'^2_{IS}}{\Sigma'^2 + \omega'^2_{IS}} \sin^2 \frac{\sqrt{\Sigma'^2 + \omega'^2_{IS}}}{2} t}_{ZQ} + \underbrace{\frac{\omega'^2_{IS}}{\Delta'^2 + \omega'^2_{IS}} \sin^2 \frac{\sqrt{\Delta'^2 + \omega'^2_{IS}}}{2} t}_{DQ}\right]. \tag{A7}$$

Part-2

II Invariance of *I*-spin Hamiltonian under the unitary transformations $\hat{U}_1\hat{U}_2$:

The RF Hamiltonian for the I-spin system is represented as

$$\hat{H}_I^{RF} = \omega_{1I}[\hat{S}_x^{14} + \hat{S}_x^{25} + \hat{S}_x^{36}]. \tag{A8}$$

The I-spin Hamiltonian ($\tilde{\hat{H}}_I^{RF}$) resulting from the $\hat{U}_1\Big(= \exp\Big\{ - \dfrac{i\theta_1}{\sqrt{2}}\big[- \hat{S}_y^{12} + \hat{S}_y^{23} - \hat{S}_y^{45} + \hat{S}_y^{56}\big]\Big\}\Big)$ unitary transformation is given as:

$$\tilde{\hat{H}}_I^{RF} = \hat{U}_1\hat{H}_I^{RF}\hat{U}_1^{\dagger} = \underbrace{\hat{U}_1\hat{U}_1^{\dagger}}_{\mathbb{I}}\hat{H}_I^{RF} = \hat{H}_I^{RF} \text{ as } \big[- \hat{S}_y^{12} + \hat{S}_y^{23} - \hat{S}_y^{45} + \hat{S}_y^{56}, \hat{H}_I^{RF}\big] = 0 \tag{A9}$$

Corollary 1:

$$\begin{aligned}\big[- \hat{S}_y^{12} + \hat{S}_y^{23} - \hat{S}_y^{45} + \hat{S}_y^{56}, \hat{H}_I^{RF}\big] &= \big[- \hat{S}_y^{12}, \hat{H}_I^{RF}\big] + \big[\hat{S}_y^{23}, \hat{H}_I^{RF}\big] + \big[- \hat{S}_y^{45}, \hat{H}_I^{RF}\big] + \big[\hat{S}_y^{56}, \hat{H}_I^{RF}\big] \\ &= \omega_{1I}\Big(i\big[\hat{S}_x^{15} - \hat{S}_x^{24}\big] + i\big[- \hat{S}_x^{26} + \hat{S}_x^{35}\big] - i\big[\hat{S}_x^{15} - \hat{S}_x^{24}\big] + i\big[\hat{S}_x^{26} - \hat{S}_x^{35}\big]\Big) \\ &= 0\end{aligned} \tag{A10}$$

Subsequently, the effect of second unitary transformation $\Big(\hat{U}_2 = \exp\Big\{i\frac{\pi}{2}\big[\hat{S}_y^{13} + \hat{S}_y^{46}\big]\Big\}\Big)$ on the I-spin Hamiltonian is evaluated as follows

$$\tilde{\tilde{\hat{H}}}_I^{RF} = \hat{U}_2\tilde{\hat{H}}_I^{RF}\hat{U}_2^{\dagger} = \underbrace{\hat{U}_2\hat{U}_2^{\dagger}}_{\mathbb{I}}\tilde{\hat{H}}_I^{RF} = \hat{H}_I^{RF} \text{ as } \big[\hat{S}_y^{13} + \hat{S}_y^{46}, \hat{H}_I^{RF}\big] = 0 \tag{A11}$$

Corollary 2:

$$\begin{aligned}\big[\hat{S}_y^{13} + \hat{S}_y^{46}, \hat{H}_I^{RF}\big] &= \big[\hat{S}_y^{12}, \hat{H}_I^{RF}\big] + \big[\hat{S}_y^{46}, \hat{H}_I^{RF}\big] \\ &= \omega_{1I}\Big(i\big[- \hat{S}_x^{16} + \hat{S}_x^{34}\big] + i\big[\hat{S}_x^{16} - \hat{S}_x^{34}\big] \\ &= 0\end{aligned} \tag{A12}$$

The above equations demonstrate the invariance of the I-spin Hamiltonian under unitary transformations involving S-spin operators.

$$\tilde{\tilde{\hat{H}}}_I^{RF} = \hat{U}_2\hat{U}_1\hat{H}_I^{RF}\hat{U}_1^{\dagger}\hat{U}_2^{\dagger} = \hat{U}_2\big(\tilde{\hat{H}}_I^{RF}\big)\hat{U}_2^{\dagger} = \hat{H}_I^{RF}. \tag{A13}$$

Part-3

III Description of CP dynamics in single-crystal (with specific orientation α_Q and $\beta_Q = 0°$)

In the simulations illustrated below, the CP dynamics is monitored as a function of time (or mixing time)

A Regime-I (C_Q = 20 kHz, Weak)

In the simulations illustrated in Figure S1, at lower I-spin RF amplitudes (ν_{1H} = 44 kHz) the oscillatory behavior in the CP experiments has a contribution from the SQ (dominant) and DQ matching conditions. At higher I-spin RF amplitudes (ν_{1H} = 63 kHz), the oscillations [Figure S1(b1-b3)] have contributions from both the DQ (dominant) and SQ matching conditions.

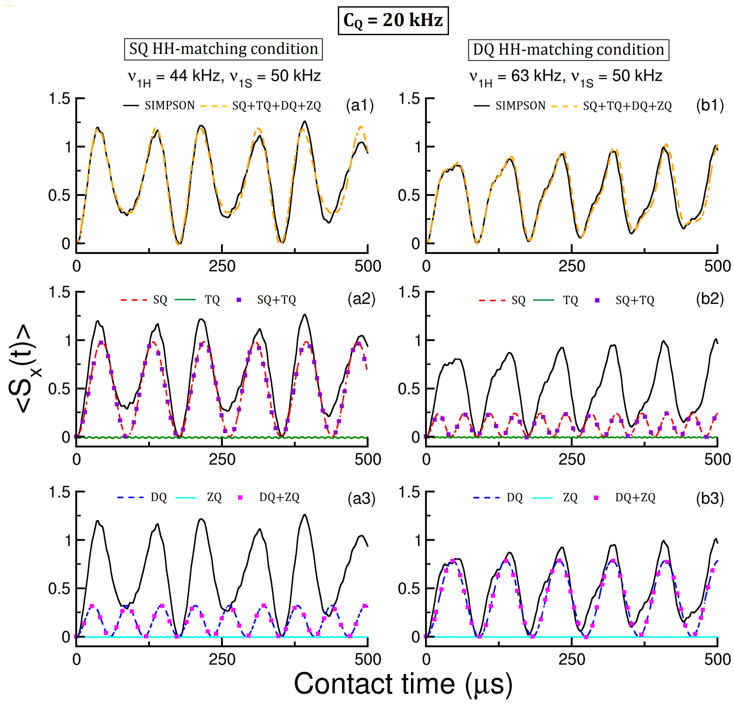

Figure S1: In the CP simulations depicted, the polarisation build-up on the S-spin (due to transfer from the I-spin) is monitored in a single crystal as a function of the CP mixing time under constant RF field strengths on both the spins. The RF amplitudes on the I-spin were chosen based on the two CP maxima observed in Figure 4 (refer to main text) i.e., panels a1-a3 (ν_{1I} = 44 kHz); panels b1-b3 (ν_{1I} = 63 kHz). The numerical simulations (based on SIMPSON) are represented by solid black lines. The following parameters were employed in the simulations: Quadrupolar parameters (C_Q = 20 kHz, η_Q = 0, quadrupolar coupling PAS angles α_Q and $\beta_Q = 0°$) and Dipolar parameters (internuclear distance r_{IS} = 1.05 Å). A constant RF amplitude of ν_{1S} = 50 kHz was employed on the quadrupole, S-spin. The analytic simulations comprising contributions from all the four CP matching conditions (SQ+TQ+DQ+ZQ) are represented in orange color. The analytic simulations based on the contributions from SQ (red), TQ (green), and SQ+TQ (indigo) are indicated separately. The analytic simulations based on the contributions from DQ (blue), ZQ (cyan) and DQ+ZQ (magenta) are indicated separately [refer to Eq. (24) in the main text].

B Regime-II ($C_Q = 200$ kHz, Intermediate)

Interestingly, in the intermediate coupling regime, at lower I-spin RF amplitudes, the dominant contributions arises from the SQ matching condition with minor contributions from the TQ matching conditions, while, contributions only from the DQ matching conditions are observed at higher RF amplitudes.

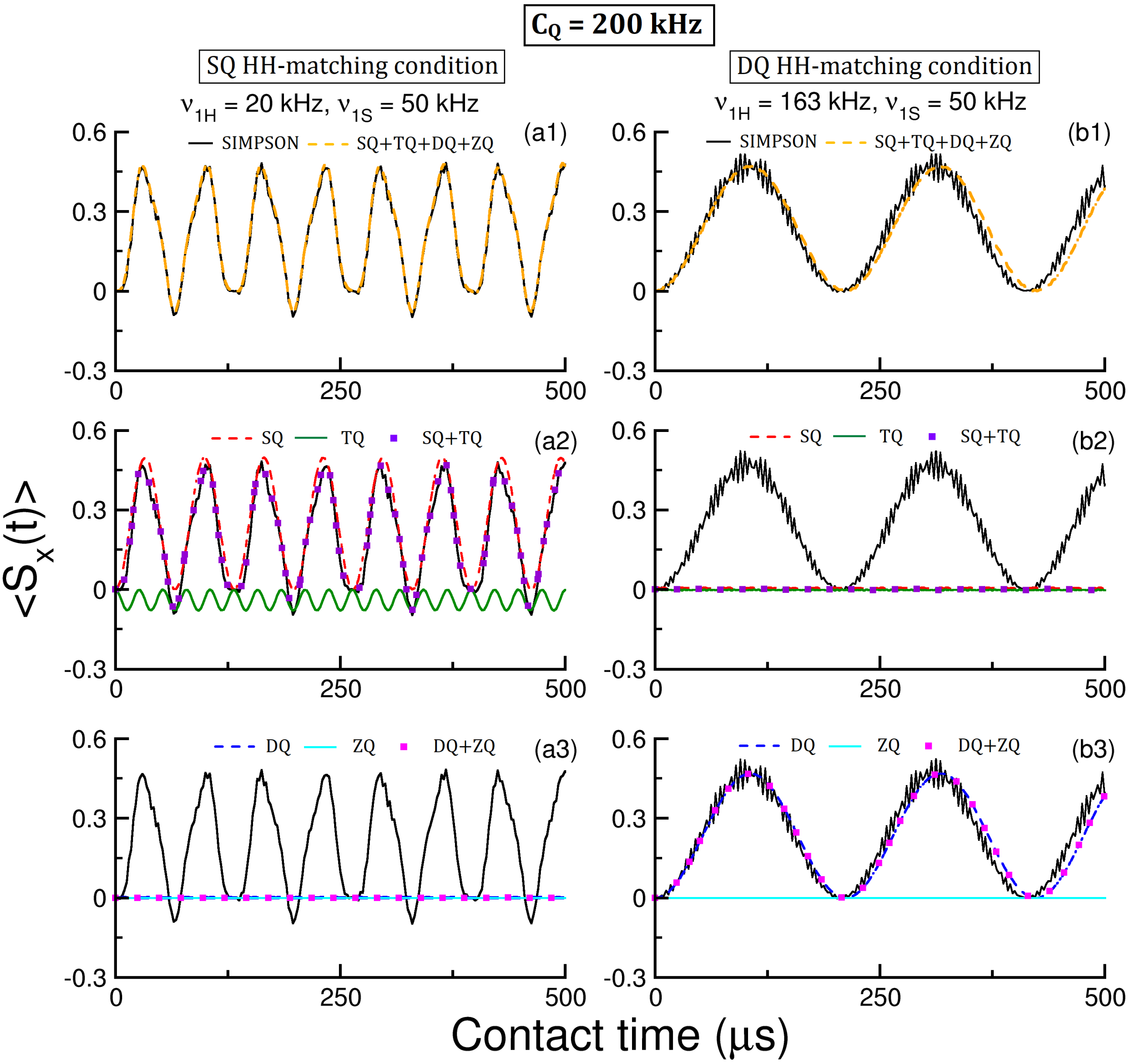

Figure S2: In the CP simulations depicted, the polarisation build-up on the S-spin (due to transfer from the I-spin) is monitored in a single crystal as a function of the CP mixing time under constant RF field strengths on both the spins. The RF amplitudes on the I-spin were chosen based on the two CP maxima observed in Figure 5 (in the main text) i.e., panels a1-a3 ($\nu_{1H} = 20$ kHz); panels b1-b3 ($\nu_{1H} = 167$ kHz). The following Quadrupolar parameters were employed in the simulations: ($C_Q =$ 200 kHz, $\eta_Q = 0$, quadrupolar coupling PAS angles α_Q and $\beta_Q = 0°$). The remaining simulation parameters and descriptions are as given in the caption of Figure S1.

C Regime-III ($C_Q = 1.0$ MHz, Strong)

In the strong coupling regime, the SQ and TQ matching condition has equal contributions at the lower RF amplitude, while only the DQ matching condition contributes at higher RF amplitudes. From a practical aspect, due to the competing nature of the SQ and TQ matching conditions, the efficiency of transfer decreases drastically in the strong coupling regime when compared to those observed in the weak and intermediate coupling regimes.

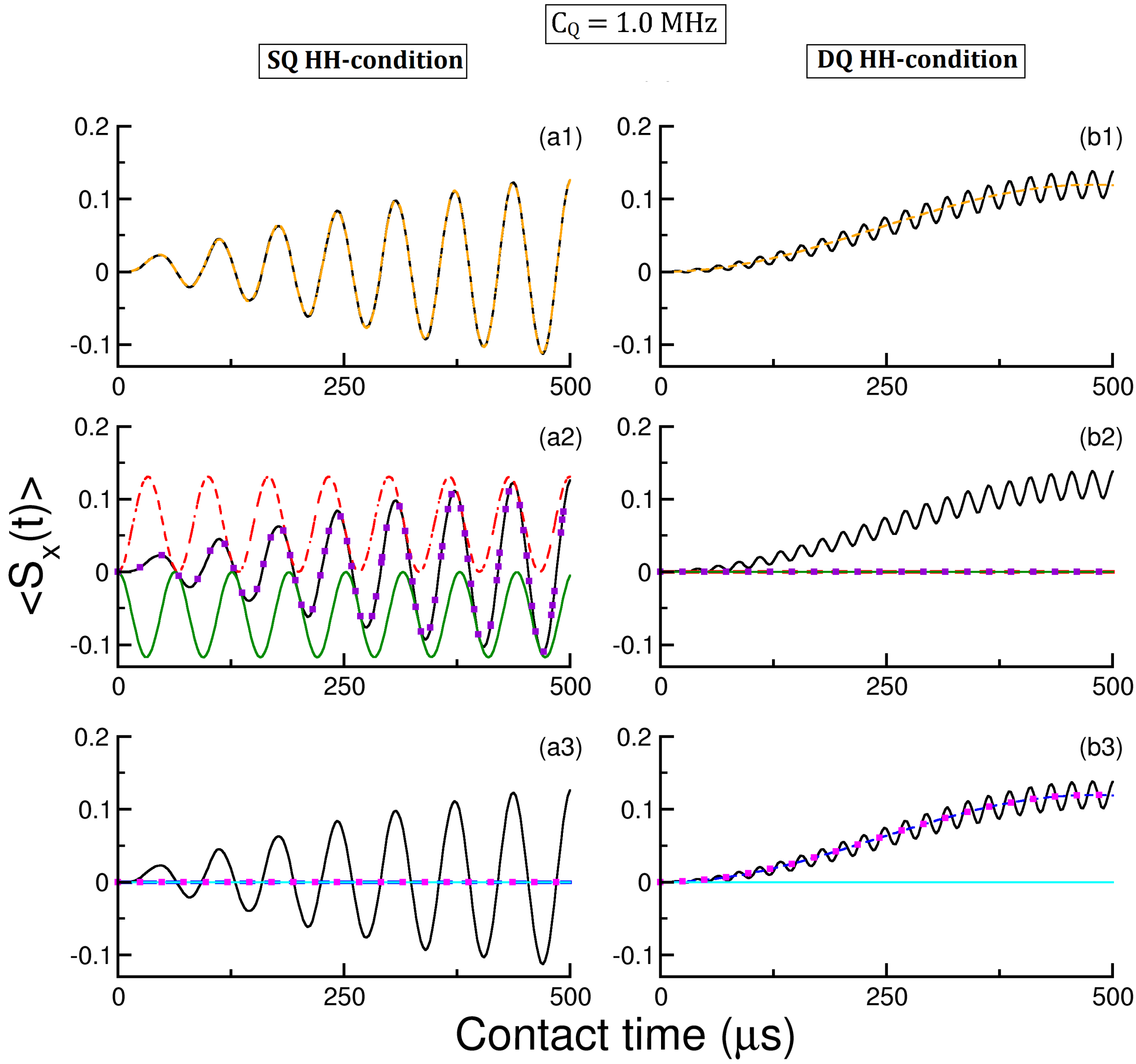

Figure S3: In the CP simulations depicted, the polarisation build-up on the S-spin (due to transfer from the I-spin) is monitored in a single crystal as a function of the CP mixing time under constant RF field strengths on both the spins. The RF amplitudes on the I-spin were chosen based on the two CP maxima observed in Figure 6 (in the main text) i.e., panels a1-a3 ($\nu_{1H} = 2$ kHz); panels b1-b3 ($\nu_{1H} = 753$ kHz). The following Quadrupolar parameters were employed in the simulations: ($C_Q = 1.0$ MHz, $\eta_Q = 0$, quadrupolar coupling PAS angles α_Q and $\beta_Q = 0°$). The remaining simulation parameters and descriptions are as given in the caption of Figure S1.

IV Role of quadrupolar spin (S) rf-field strength on CP spin dynamics

The effect of the strength of the S-spin rf field is highlighted under three different quadrupolar coupling strengths. As demonstrated by the scaling factor $4\omega_{1S}/\omega_e$ in Eq. (24) (in the main text), the CP efficiency increases with increasing S-spin rf-field strength across all quadrupolar coupling regimes. An additional increase in CP efficiency is observed at lower I-spin RF amplitudes with a decrease in the interference effects from the TQ/ZQ fields, as the strength of the S-spin rf field increases.

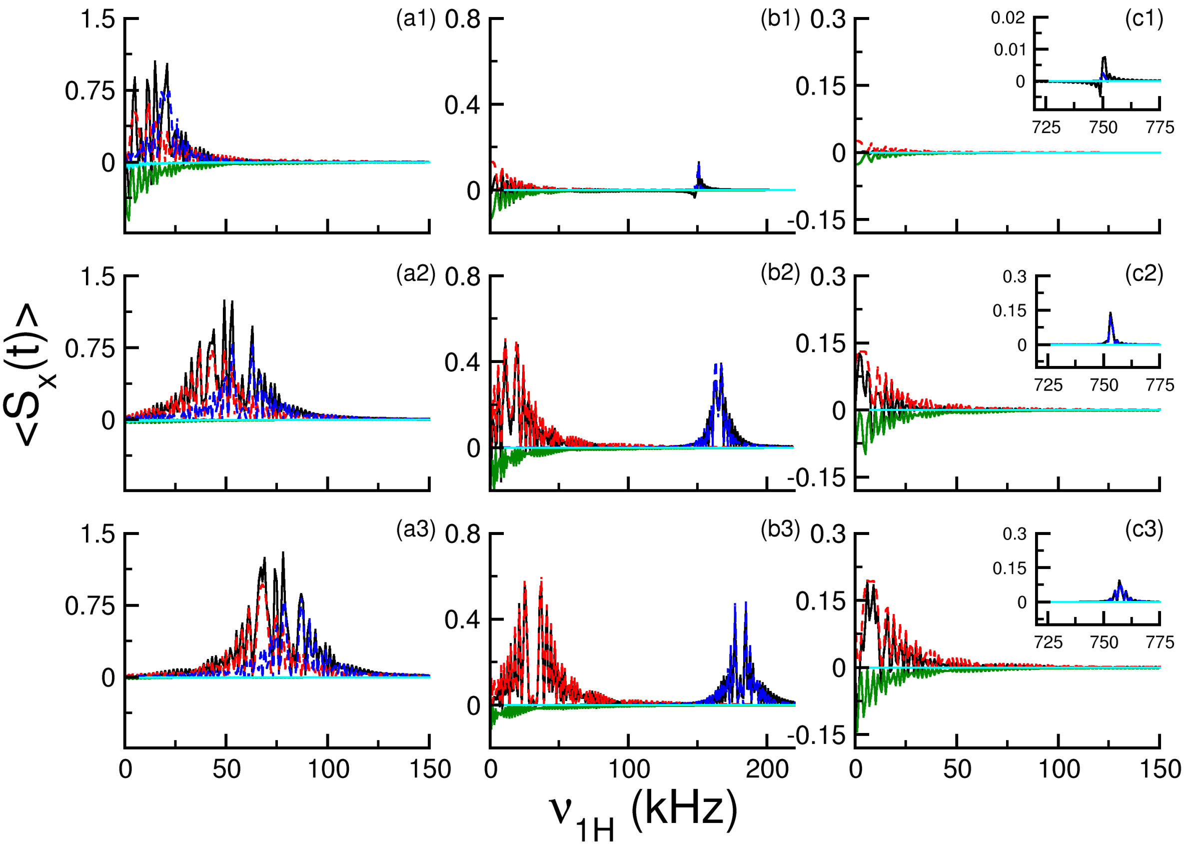

Figure S4: In the CP simulations depicted, the polarisation build-up on the S-spin (due to transfer from the I-spin) is monitored in a single crystal (with general orientation) as a function of the RF field employed on the I-spin under different S-spin rf field strength ν_{1S}: 10 kHz (a1,b1,c1), 50 kHz (a2,b2,c2) and 75 kHz (a3,b3,c3). The numerical simulations (based on SIMPSON) are represented by solid black lines. The following parameters were employed in the simulations: Quadrupolar parameters (C_Q = 20 kHz (a1-a3), 200 kHz (b1-b3), and 1.0 MHz (c1-c3), $\eta_Q = 0$, quadrupolar coupling PAS angle α_Q and $\beta_Q = 0°$), Dipolar parameters (inter-nuclear distance $r_{IS} = 1.05$ Å) and the mixing time during the CP experiment was held constant (say $t_{mix} = 0.5$ ms). The analytic simulations based on signal expressions corresponding to various CP matching conditions are indicated: SQ (red), TQ (green), DQ (blue) and ZQ (cyan) [refer to Eq. (24) in the main text]. The insets in panels c1-c3 show CP maxima in the higher I-spin RF field range.

V CP dynamics in single-crystal (general orientation)

To outline the orientation dependence of the quadrupolar interactions in CP experiments, additional simulations in single-crystal with general orientations were also carried out. As illustrated in Eq. (2) (refer to main text), the quadrupolar interaction depends on the Euler angles (α_Q and β_Q). In the quadrupolar principal axis frame the angle β_Q denotes the angle between the static magnetic field and the z-axis of the quadrupolar PAS, while, α_Q represents its projection along the x-y plane.

In the simulation depicted in Figure S5, the relative contributions from the four matching conditions are presented for a set of eight β_Q angles in the range $0° \leq \beta_Q \leq 180°$. As depicted in Figure S5, when β_Q is less than 54.736 ($0° \leq \beta_Q < 54.736°$), the CP profile approaches the weak coupling regime and the CP efficiency improves. At $\beta_Q = 54.736°$, the quadrupolar interaction reduces to zero (for a symmetric tensor, $\eta_Q = 0$) and the trajectories emerging from the SQ and DQ matching conditions overlap. This observation could also be substantiated through the analytic expression given in Eq. (24) (in the main text). From an experimental perspective, the interesting observation emerges for cases where the angle β_Q in the range ($54.736° < \beta_Q < 125.264°$). As illustrated in the simulations (refer to panels a4-a6), the CP profile approaches the intermediate coupling regimes along with swapping in the position of the CP matching conditions due to the negative sign of ω_Q in the above range of β_Q. We observe a profound change in the relative contributions from the four CP matching conditions. As depicted, at lower I-spin RF amplitudes, the CP profile has a dominant contribution from the DQ/ZQ CP matching condition, while at higher I-spin RF amplitudes, the SQ matching condition contributes with negligible contribution from the TQ condition. This trend is completely opposite to those depicted in the weak (Figure 4), intermediate (Figure 5), and strong (Figure 6) coupling regimes in the main text. At $\beta_Q = 125.264°$, the quadrupolar interaction reduces to zero for a symmetric tensor, and the CP profile is similar to the one observed at $\beta_Q = 54.736°$. From $125.264° \leq \beta_Q \leq 180°$, the CP profile resembles to the one obtained for β_Q in the range $54.736° \geq \beta_Q \geq 0°$. Interestingly, the relative contributions from the four matching conditions are reversed (in contrast to those observed in the range, $54.736° < \beta_Q < 125.264°$) and is in accord with those depicted in the earlier simulations (please refer to Figures 4, 5, and 6 in the main text). Hence the value of β_Q plays an important role in quantifying the CP profile in terms of four matching conditions and highlights the non-uniformity of the CP transfer among different quadrupolar tensor orientations. The shift in positions of SQ/TQ and DQ/ZQ resonances with the variation of PAS β_Q angle depends strongly on the size of quadrupolar coupling strength C_Q. For instance, the variation of β_Q angle for $C_Q = 20$ kHz (refer to Figure S6) shows a similar pattern as discussed above, however, the change in positions of these resonances are not huge in comparison to those depicted in Figure S5. The quadrupolar PAS angle α_Q affects the magnitude of the quadrupolar frequency (not sign for $\beta_Q = 90°$) in the case of asymmetric tensor and is shown in Figure S7.

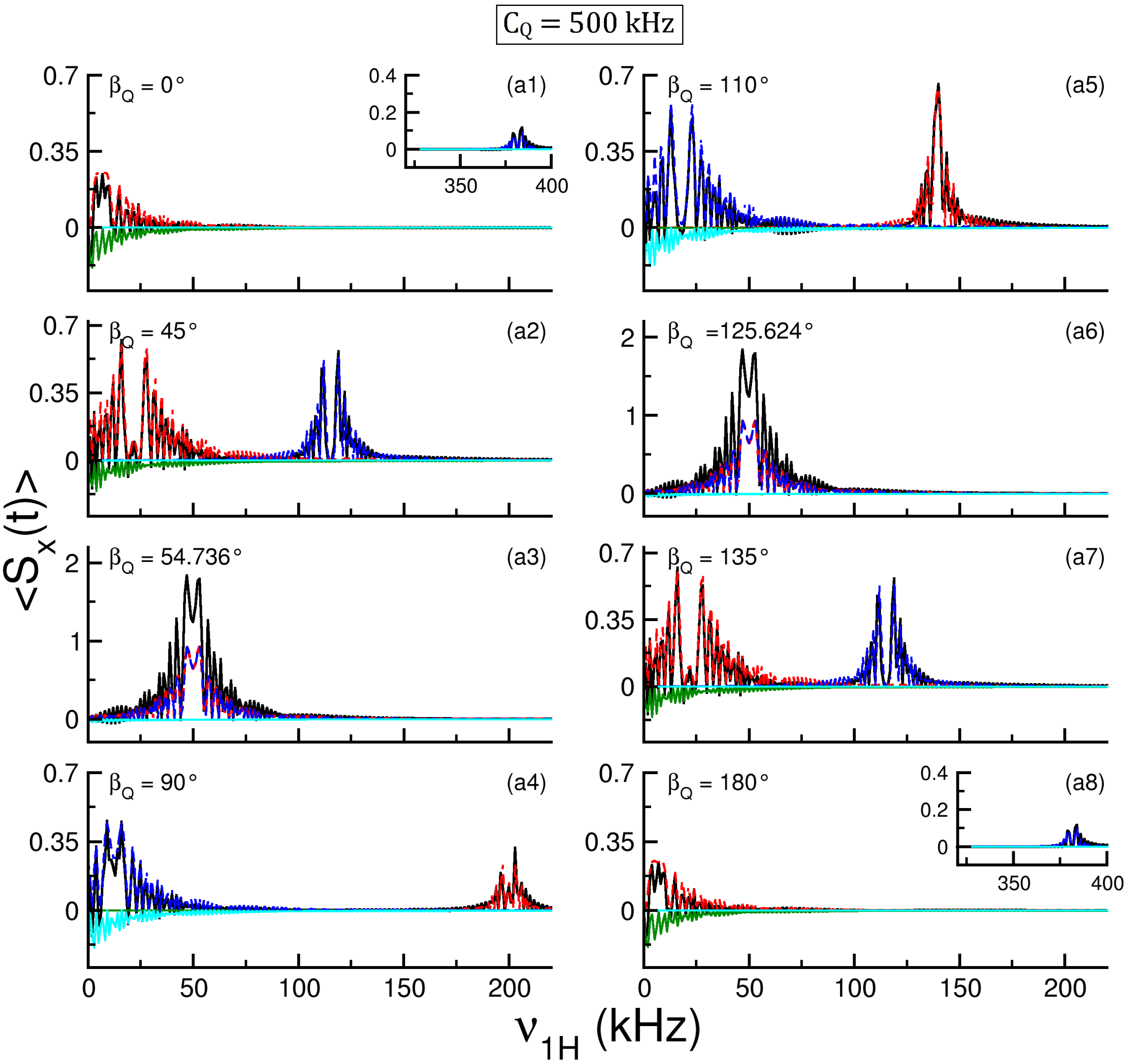

Figure S5: In the CP simulations depicted, the polarisation build-up on the S-spin (due to transfer from the I-spin) is monitored in a single crystal (with general orientation) as a function of the RF field employed on the I-spin. The numerical simulations (based on SIMPSON) are represented by solid black lines. In the simulations depicted, the effects of the variation of quadrupolar coupling PAS angle β_Q: 0° (a1), 45° (a2), 54.736° (a3) 90° (a4), 110° (a5), 125.624° (a6), 135° (a7) and 180°(a8) on the CP dynamics is illustrated. The following parameters were employed in all the simulations: $C_Q = 500$ kHz, $\eta_Q = 0$, quadrupolar coupling PAS angle $\alpha_Q = 0°$, contact time $(t_{mix}) = 0.5$ ms, inter-nuclear distance $r_{IS} = 1.05$ Å and $\nu_{1S} = 50$ kHz. The analytic simulations based on signal expressions corresponding to various CP matching conditions are indicated: SQ (red), TQ (green), DQ (blue) and ZQ (cyan) [refer to Eq. (24) in the main text]. The insets in panels a1 and a8 show CP maxima in the higher I-spin RF field range.

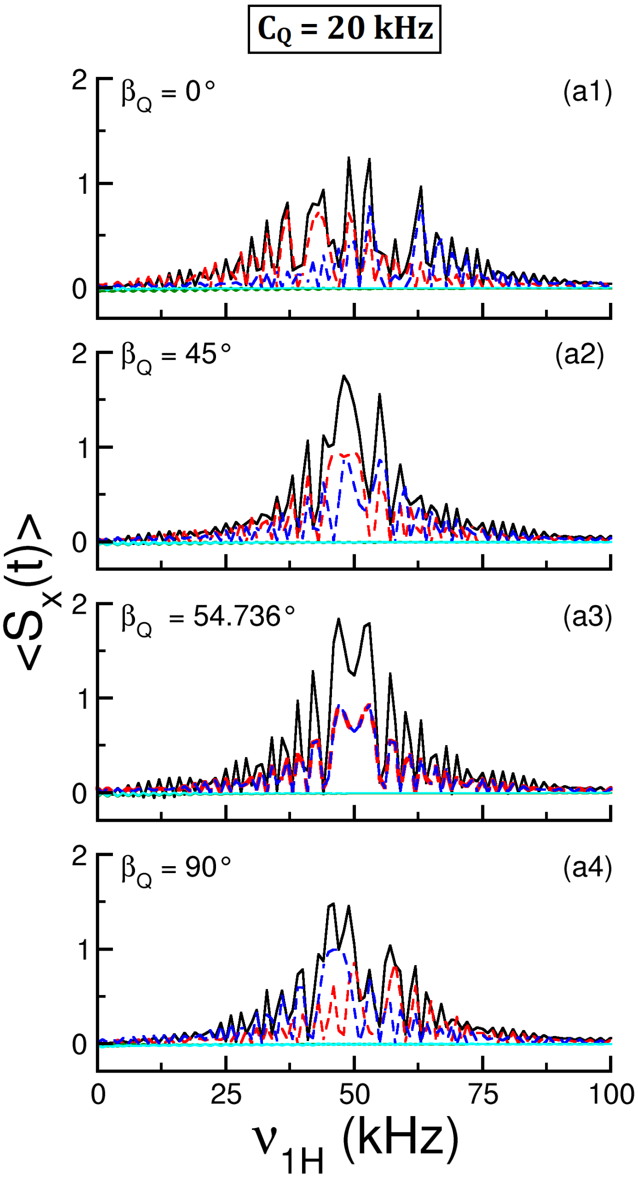

Figure S6: In the CP simulations depicted, the polarisation build-up on the S-spin (due to transfer from the I-spin) is monitored in a single crystal (with general orientation) as a function of the RF field employed on the I-spin. The numerical simulations (based on SIMPSON) are represented by solid black lines. In the simulations depicted, the effects of the variation of quadrupolar coupling PAS angle β_Q: 0° (a1), 45° (a2), 54.736° (a3) and 90° (a4) on the CP dynamics are illustrated. The following parameters were employed in all the simulations: $C_Q = 20$ kHz, $\eta_Q = 0$, quadrupolar coupling PAS angle $\alpha_Q = 0°$, contact time $(t_{mix}) = 0.5$ ms, inter-nuclear distance $r_{IS} = 1.05$ Å and $\nu_{1S} = 50$ kHz. The analytic simulations based on signal expressions corresponding to various CP matching conditions are indicated, SQ (red), TQ (green), DQ (blue) and ZQ (cyan) [refer to Eq. (24) in the main text].

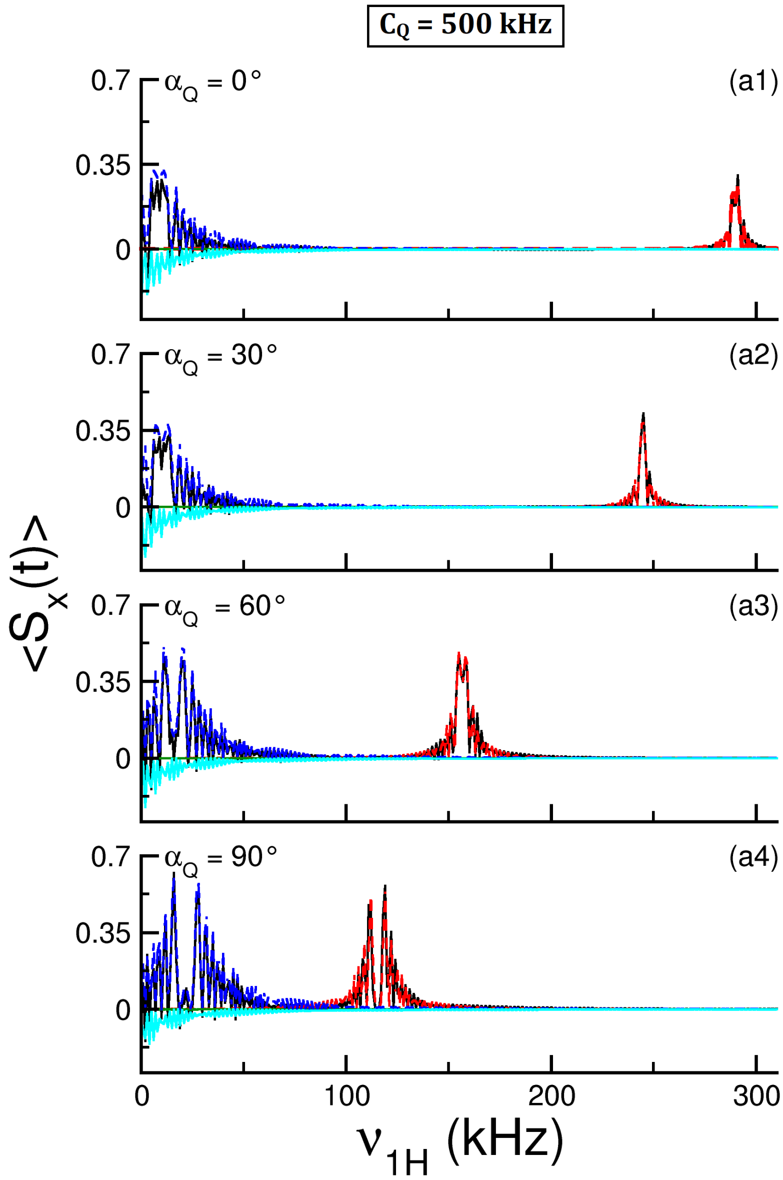

Figure S7: In the CP simulations depicted, the polarisation build-up on the S-spin (due to transfer from the I-spin) is monitored in a single crystal (with general orientation) as a function of the RF field employed on the I-spin. The numerical simulations (based on SIMPSON) are represented by solid black lines. In the simulations depicted, the effects of the variation of quadrupolar coupling PAS angle α_Q: 0° (a1), 30°$(a2)$, 60° (a3) and 90° (a4) on the CP dynamics are illustrated. The following parameters were employed in all the simulations: $C_Q = 500$ kHz, $\eta_Q = 0.5$, quadrupolar coupling PAS angle $\beta_Q = 90°$, contact time $(t_{mix}) = 0.5$ ms, inter-nuclear distance $r_{IS} = 1.05$ Å and $\nu_{1S} = 50$ kHz. The analytic simulations based on signal expressions corresponding to various CP matching conditions are indicated, SQ (red), TQ (green), DQ (blue) and ZQ (cyan) [refer to Eq. (24) in the main text]

VI Description of the CP dynamics in powder sample

In contrast to the CP dynamics in single crystal, the CP mixing time profile in a powder sample has complicated dependence on the four matching conditions. This aspect is further validated in the simulations depicted in Figure S8. With increasing quadrupolar coupling strength, the time-domain oscillations become wiggled due to the interplay of various CP fields, therefore representing a complex CP transfer mechanism.

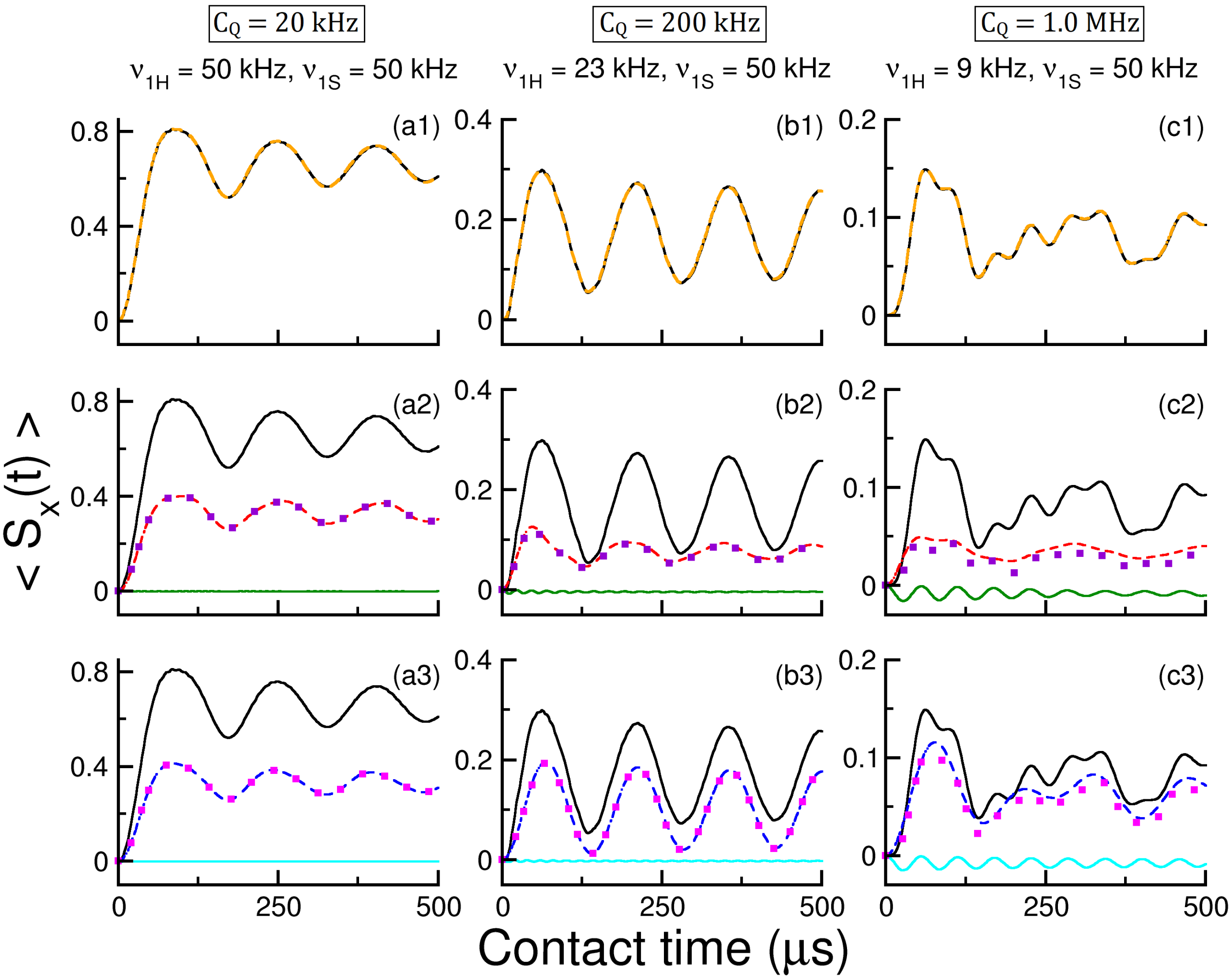

Figure S8: In the CP simulations depicted, the polarisation build-up on the S-spin (due to transfer from the I-spin) is monitored in a powder sample as a function of the CP mixing time under constant RF amplitudes on the spins. The RF amplitudes on the I-spin were chosen based on the two CP maxima observed in Figure 7 (in the main text) i.e., panels a1-a3 ($\nu_{1H} = 50$ kHz); panels b1-b3 ($\nu_{1H} = 23$ kHz); panels c1-c3 ($\nu_{1H} = 9$ kHz). The following parameters were employed in the simulations: panels a1-a3 ($C_Q = 20$ kHz, $\eta_Q = 0$); panels b1-b3 ($C_Q = 200$ kHz, $\eta_Q = 0$) and panels c1-c3 ($C_Q = 1.0$ MHz, $\eta_Q = 0$). The remaining simulation parameters and descriptions are as given in the caption of Figure S1. The powders simulations were performed using 4180 orientations (i.e., $zcw4180$) of α and β.

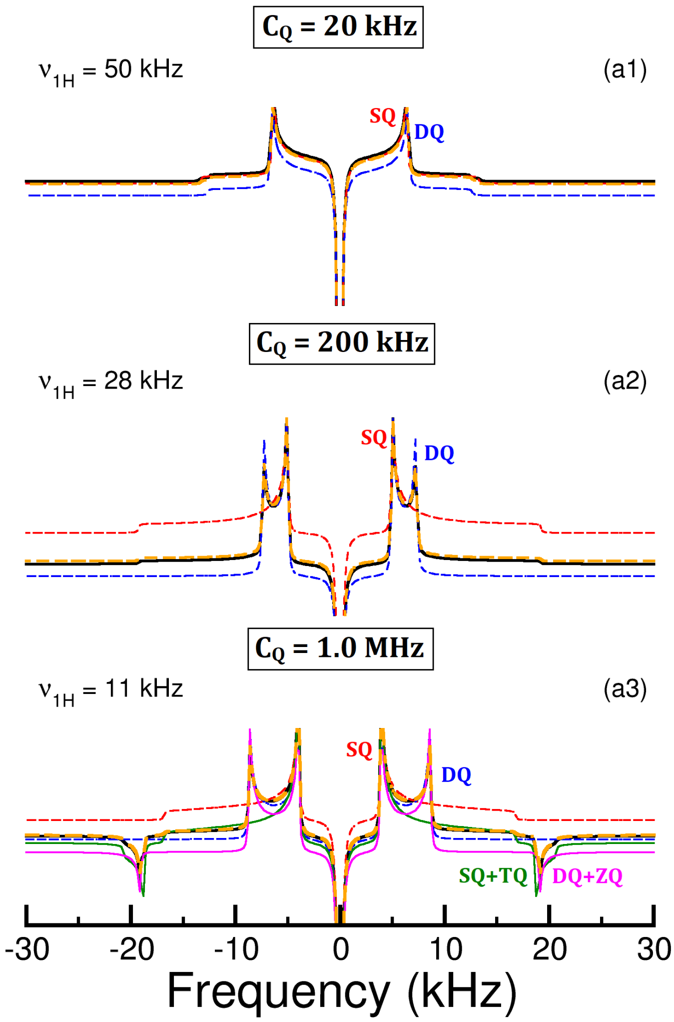

Figure S9: In the simulations depicted, the frequency-domain individual S-spin CP signals in a powder sample emerging from the Fourier transformation of the mixing time domain signal is depicted for different quadrupolar coupling constants: panel a1 (C_Q = 20 kHz); panel a2 (C_Q = 200 kHz) and panel a3 (C_Q = 1.0 MHz). All other parameters such as the quadrupolar coupling PAS angles α_Q and $\beta_Q = 0°$, dipolar parameters (inter-nuclear distance $r_{12} = 1.05$ Åand dipolar PAS angle $\theta = 0°$) and RF amplitude of S-spin $\nu_{1S} = 50$ kHz were identical in all the simulations. Depending on the magnitude of the quadrupolar coupling constant, the RF amplitudes employed on the I-spin (indicated in the Figure) were carefully selected by CP in maxima of the rf-domain simulation at the desired contact time. The numerical simulations (based on SIMPSON) are represented by solid black lines. The analytic simulations in the panels have the following definitions: the analytic simulations comprise contributions from all the four CP matching conditions (SQ+TQ+DQ+ZQ) and is represented in orange color and the analytic simulations based on the contributions SQ (red), SQ+TQ (green), DQ (blue) and DQ+ZQ (magenta) are depicted [based on Eq. (24) in the main text]. The powders simulations were performed using 4180 orientations (i.e., $zcw4180$) of α and β. A line broadening of 50 Hz was used before the Fourier transform of the time-domain CP signal.